NAVAL
POSTGRADUATE
SCHOOL

MONTEREY, CALIFORNIA

THESIS

ENHANCED IONIZATION OF PROPELLANT THROUGH CARBON NANOTUBE GROWTH ON ANGLED WALLS

by

Alfred P. Garvey

June 2017

Thesis Advisor:	Dragoslav Grbovic
Second Reader:	Fabio Alves

THIS PAGE INTENTIONALLY LEFT BLANK

REPORT DOCUMENTATION PAGE

Form Approved OMB No. 0704–0188

Public reporting burden for this collection of information is estimated to average 1 hour per response, including the time for reviewing instruction, searching existing data sources, gathering and maintaining the data needed, and completing and reviewing the collection of information. Send comments regarding this burden estimate or any other aspect of this collection of information, including suggestions for reducing this burden, to Washington headquarters Services, Directorate for Information Operations and Reports, 1215 Jefferson Davis Highway, Suite 1204, Arlington, VA 22202-4302, and to the Office of Management and Budget, Paperwork Reduction Project (0704-0188) Washington, DC 20503.

1. AGENCY USE ONLY (Leave blank)	2. REPORT DATE June 2017	3. REPORT TYPE AND DATES COVERED Master's thesis

4. TITLE AND SUBTITLE
ENHANCED IONIZATION OF PROPELLANT THROUGH CARBON NANOTUBE GROWTH ON ANGLED WALLS

5. FUNDING NUMBERS

6. AUTHOR(S) Alfred P. Garvey

7. PERFORMING ORGANIZATION NAME(S) AND ADDRESS(ES)
Naval Postgraduate School
Monterey, CA 93943-5000

8. PERFORMING ORGANIZATION REPORT NUMBER

9. SPONSORING /MONITORING AGENCY NAME(S) AND ADDRESS(ES)
N/A

10. SPONSORING / MONITORING AGENCY REPORT NUMBER

11. SUPPLEMENTARY NOTES The views expressed in this thesis are those of the author and do not reflect the official policy or position of the Department of Defense or the U.S. Government. IRB number ____N/A____.

12a. DISTRIBUTION / AVAILABILITY STATEMENT
Approved for public release. Distribution is unlimited.

12b. DISTRIBUTION CODE

13. ABSTRACT (maximum 200 words)

A benchmark to compare ion thrusters is the mass utilization factor (MUF). The MUF is the ratio of the ionization area to the total cross-sectional area of the thruster and is proportional to the amount of propellant gas that is ionized to produce thrust; a higher MUF means greater thrust generated. Previous work has shown that the mass utilization factor of a carbon nanotube (CNT)–coated angled nozzle is much higher in respect to a 2-dimensional configuration of the same. In other words, stacking concentric square rings of decreasing size would result in much more propellant being ionized than a thruster of constant width.

In this thesis, several important benchmarks were set. First, building upon previous thesis work, an angled sidewall was etched into a silicon wafer, resulting in an equation that can be utilized to achieve different angles. Second, that etching process was able to be applied long enough to create a nozzle through the silicon wafer. Third, after successfully growing CNTs on the angled side walls of the nozzle, a mass utilization factor was calculated from the etched nozzle. Lastly, a method for calculating an "ideal" MUF (based on current modelling) was fashioned to provide a baseline comparison to future laboratory testing.

14. SUBJECT TERMS
carbon nanotubes, ion thrusters, mass utilization factor

15. NUMBER OF PAGES
61

16. PRICE CODE

17. SECURITY CLASSIFICATION OF REPORT	18. SECURITY CLASSIFICATION OF THIS PAGE	19. SECURITY CLASSIFICATION OF ABSTRACT	20. LIMITATION OF ABSTRACT
Unclassified	Unclassified	Unclassified	UU

THIS PAGE INTENTIONALLY LEFT BLANK

**ENHANCED IONIZATION OF PROPELLANT THROUGH CARBON
NANOTUBE GROWTH ON ANGLED WALLS**

Alfred P. Garvey
Ensign, United States Navy
B.S., United States Naval Academy, 2016

Submitted in partial fulfillment of the
requirements for the degree of

MASTER OF SCIENCE IN PHYSICS

from the

**NAVAL POSTGRADUATE SCHOOL
June 2017**

Approved by: Dragoslav Grbovic, Ph.D.
Thesis Advisor

Fabio Alves, Ph.D.
Second Reader

Kevin B. Smith, Ph.D.
Chair, Department of Physics

THIS PAGE INTENTIONALLY LEFT BLANK

ABSTRACT

A benchmark to compare ion thrusters is the mass utilization factor (MUF). The MUF is the ratio of the ionization area to the total cross-sectional area of the thruster and is proportional to the amount of propellant gas that is ionized to produce thrust; a higher MUF means greater thrust generated. Previous work has shown that the mass utilization factor of a carbon nanotube (CNT)–coated angled nozzle is much higher in respect to a 2-dimensional configuration of the same. In other words, stacking concentric square rings of decreasing size would result in much more propellant being ionized than a thruster of constant width.

In this thesis, several important benchmarks were set. First, building upon previous thesis work, an angled sidewall was etched into a silicon wafer, resulting in an equation that can be utilized to achieve different angles. Second, that etching process was able to be applied long enough to create a nozzle through the silicon wafer. Third, after successfully growing CNTs on the angled side walls of the nozzle, a mass utilization factor was calculated from the etched nozzle. Lastly, a method for calculating an "ideal" MUF (based on current modelling) was fashioned to provide a baseline comparison to future laboratory testing.

THIS PAGE INTENTIONALLY LEFT BLANK

TABLE OF CONTENTS

THIS PAGE INTENTIONALLY LEFT BLANK

LIST OF FIGURES

LIST OF TABLES

THIS PAGE INTENTIONALLY LEFT BLANK

LIST OF ACRONYMS AND ABBREVIATIONS

CNT	carbon nanotube
CRT	cathode ray tube
CVD	chemical vapor deposition
DS1	Deep Space 1
EP	electric propulsion
FEEP	field emission electric propulsion
MUF	mass utilization factor
NSTAR	NASA Solar Technology Application Readiness
SCATHA	Spacecraft Charging at High Altitudes
SEM	scanning electron microscope
TMDE	time-multiplexed deep etching
UV	ultraviolet

THIS PAGE INTENTIONALLY LEFT BLANK

ACKNOWLEDGMENTS

THIS PAGE INTENTIONALLY LEFT BLANK

I. INTRODUCTION AND BACKGROUND

A. ELECTRIC PROPULSION BASICS

Electric propulsion (EP) uses the same basic principles of thrust as conventional jet engines: the acceleration of mass out of the rear of the nozzle creates a force in the forward direction, but instead of using combustion to accelerate the air particles, EP uses electricity to accelerate propellant particles [1].

EP thrusters come in several different types. The first, and most rudimentary, of which developed along with the cathode ray tube (CRT) [2]. The filament inside a vacuum is heated resulting in emitted electrons; the electrons (produced at the cathode) are then accelerated towards a positive anode [3]. This type of thruster was first conjectured by Konstatantin Tsiolkovsky in the early 20th century [2]. He measured the exhaust velocities of electron flux resulting from CRTs and saw that he was getting particle velocities 6,000 to 20,000 times greater than contemporary (at the time) combustion methods. Tsiolkovsky's work on electron velocities paralleled his work with rocket exhaust velocities. Later on in his work, he saw the potential for the use of EP in space but was unable to see it come to fruition.

A second type of EP thruster is electrostatic propulsion. This differs slightly from the CRTs because instead of only accelerating electrons (their low mass results in very little forward momentum) it uses electric fields to accelerate any charged propellant [4]. The electrostatic subsection of EP was pioneered by Robert Goddard [2]. He stated that voltage differences could be used to accelerate electrons close to the speed of light. He created what he called the "Method of and Means for Producing Electrified Jets of Gas," which showed a method of electrostatic ion acceleration to be used for propulsion specifically. That was as far as he ventured, due to the greater current demand for chemical rocket propulsion. In addition to electrostatic propulsion, electrothermal (the use

of electrical heating to expand propellant and accelerate it through the nozzle) propulsion, and electromagnetic (the use of electric and magnetic fields to ionize propellant gas and direct resulting plasma) also exist [4].

Sutton and Biblarz wrote on how ion propulsion is much more effective than electron propulsion because of the more massive propellant and is generally utilized via electrostatic and electromagnetic propulsion. Electrostatic propulsion can be split into two separate categories: electron bombardment and field emission. In electron bombardment, as the name suggests, free electrons bombard neutrally charged gas propellant particles. The resulting positively charged ions are accelerated towards a negatively charged grid creating thrust in the opposite direction. Field emission electric propulsion (FEEP) works differently. FEEP thrusters take advantage of the very high electric fields that surround sharp points by sending liquid metal across them ionizing the liquid propellant; the low resultant thrust is applicable for satellite station keeping operations [1].

An example of an electromagnetic thruster is the Hall effect thruster. Cross-field discharge, as outlined in the Hall effect, is used to create a plasma [1]. An applied magnetic field results in a perpendicular electric field. The electric field then accelerates the ions in the plasma resulting in high exhaust velocities [1]. This method is effective because the applied magnetic field protects the system from shorting out due to electron motion [1]. The efficiency of Hall Effect thrusters overall are lower than comparable ion thrusters but are able to outperform them at certain power levels [1]. Another benefit is the relatively simple production of the devices [1]. In the general case, Hall Effect thrusters are electromagnetic in nature, if an electron current transverse to the ion flow is used to neutralize the ion accelerating region, it can be categorized as an electrostatic thruster [4].

B.   MODERN TECHNOLOGICAL APPLICATIONS

The technology pioneered by Goddard, Tsiolkovsky, and others laid the groundwork for a plethora of modern technologies. The uses include the charging of spacecraft and several iterations of ion propulsion.

1.   Spacecraft Charging at High Altitudes Experiments

This experiment, Spacecraft Charging at High Altitudes (SCATHA), was developed by the U.S. Air Force along with NASA [5]. A satellite was launched into geosynchronous orbit to perform several tests at various densities of plasma in the high altitude atmosphere as well as during an eclipse [5]. The experiment made use of electron beams, akin to those studied by Tsiolkovsky, to study the basic plasma processes, vehicle charging, magnetospheric fields/structures and the interaction between ambient plasma and the electron beam in the ionosphere and magnetosphere [5]. When the electron beam was in use and the beam current was high enough, the overall electric potential of the satellite increased [5]. The potential also increased because of interactions between the electron beam and the surrounding electrons in the atmosphere [5]. The understanding of these interactions as well as the mitigation of the net positive charge increase resulting from beam operations that prevented negative effects to satellite operations came from the early work in electron propulsion and ion propulsion.

2.   Deep Space 1

The low fuel cost of electrostatic ion propulsion, as predicted by the early pioneers of the field, has resulted in its use in several long-range space crafts. NASA's Deep Space 1 (DS1) used inert xenon gas as fuel in its xenon ion propulsion system (XIPS) [4].

Figure 1 shows how the XIPS was utilized on the DS1 spacecraft; it operated on input power ranging from 0.5-3.3kW and produced 19–92mN of thrust over specified impulses: 1900s at 0.5kW to 3100s at 2.3kW [6]. Launched on October 24, 1988, the DS1 spacecraft would travel roughly 1.5 billion miles on

an intercept path with the Borrelly comet, testing a concentrated solar array, communications equipment, autonomous optical navigation, imaging spectrometers, and of course, the XIPS [7]. The DS1 performed above initial expectations, spending 1,151 days in operation in deep space and logging 16,246 hours of use on the XIPS with the total fuel usage of only 72kg [7].
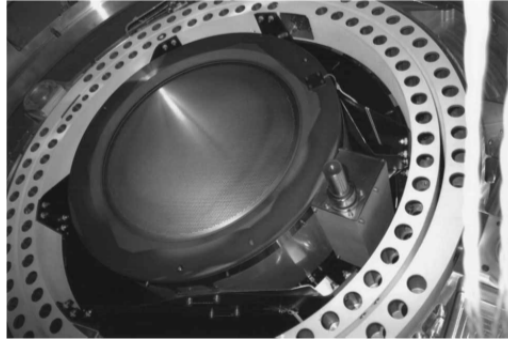
Figure 1. Xenon ion propulsion system, gimbal mounted and deployed on DS1. Source: [6].

3. DAWN

A more recent use of XIPS is the DAWN Spacecraft from NASA. Orbiting the dwarf planet Ceres, DAWN utilizes 3 XIPS engines, although only using 1 at a time, producing a thrust of 91mN comparable to that of the DS1 spacecraft [8] [9]. The expected use of the XIPS on the DAWN is 2,100 days [9]. During its lifetime, DAWN will inspect two protoplanets in the asteroid belt that are particularly interesting due to them remaining intact since formation [8]. The completion of this mission, the major obstacle being repositioning a spacecraft in deep space, is only possible through the extreme efficiency of ion propulsion, illustrating the applications and opportunities for further advancement in the field [8]. In the scope of this project, it is the field of ion thruster miniaturization.

C. PREVIOUS WORK IN ION THRUSTER MINIATURIZATION

Much like the FEEP system discussed prior, carbon nanotubes (CNT) can be used to create very high and very local electric fields to ionize propellant.

Thus, in order for the propellant to be ionized the molecules must pass close enough to interact with the local electric field [10].

As propellant gas passes by the CNT tip, as shown in Figure 2, some molecules may become ionized depending on their distance from the CNT tip. Expectedly, not all of the gas would become ionized. A metric for comparing the efficiency of a miniaturized ion thruster would be the amount of gas propellant that is ionized in relation to the total gas propellant used. Jarrod Ozereko studied this idea and evaluated the ion thrusters based on a Mass Utilization Factor (MUF), which is the ratio of the effective area of the thruster that would be able to ionize incoming propellant to the overall area of the thruster [11]. Ozereko was able to calculate this effective area of ionization based on a minimum and maximum distance from the carbon nanotube tip in relation to the diameter of his circular opening [11]. Through experiments he measured his MUF to be 0.036%, lower than his calculated 0.052% [11]. He provided two hypotheses to better the MUF: decrease the size of the openings and layering the 2-D rings to create a nozzle [11].

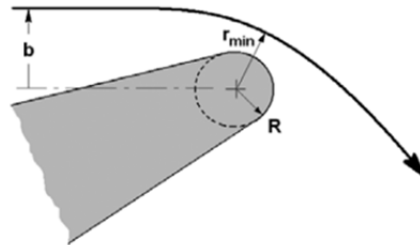Figure 2. Schematic of the interaction between propellant gas and CNT tip. Source: [12].

Brandi Gilbert, in her thesis, set to expand on Ozereko's work and sought to study the effect of a square opening and the fabrication of a nozzle structure on the MUF. She found that the minimum distance of ionization was actually inside the radius of the CNT tip [10]. Using Ozereko's method of calculating

5

MUF, she found that her single square opening had an MUF of 0.040% [10]. Although this is less than Ozereko's original estimate, the difference can be accounted for in the differences in areas of the openings [10]. Gilbert also sought to study the effect of angled walls on propellant ionization but did not achieve producing the angled cross section of the nozzle. Instead, she took a flat walled nozzle and using a 45 degree sample holder was able to model and grow carbon nanotubes on the angled wall [10].

Using the schematic shown in Figure 3, Gilbert was able to calculate a cumulative MUF for the nozzle of 0.164%, a 410% increase over the original calculations [10].
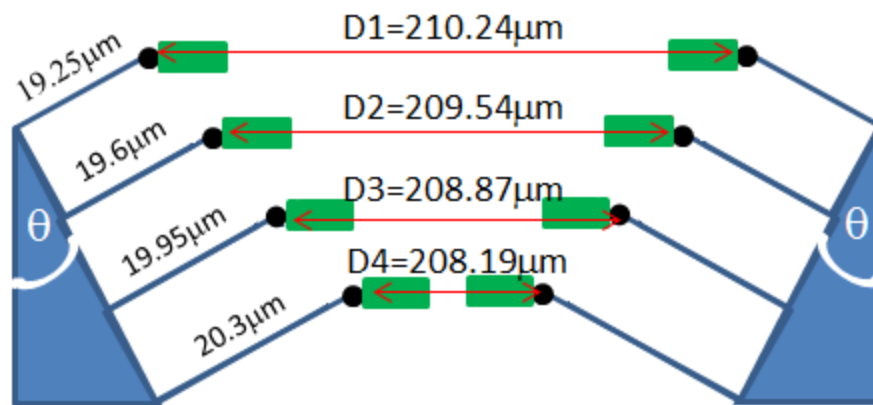
A schematic model of one CNT per ring of Gilbert's final results with the green area being the effective ionization area.

Figure 3. CNT arrangement with measurements at 45-degree angle.
Source: [10].

This thesis will expand on the concepts discussed previously, specifically seeking to successfully etch a nozzle with angled walls, grow carbon nanotubes in parallel process on the multitude of angled-walled nozzle and calculate the resultant MUF with a secondary focus on streamlining the process of fabrication, adjustment, and integration of samples into a laboratory test setting.

II. EXPERIMENTAL PROCEDURE

A. GENERAL OVERVIEW

The fabrication of nozzles with CNTs is a multi-step process. First the sample is prepared for etching, then is etched through creating the array of nozzles, next the nozzle array is primed for CNT growth, finally the array is placed in the furnace where CNTs are grown on the angled walls.

Figure 4 shows a rough graphical outline of the nozzle fabrication process, with the cross section of a single nozzle depicted. It begins as a blank silicon wafer with a layer of silicon dioxide on both sides. The silicon dioxide helps reinforce the lithographic mask of the nozzle and preserve the desired angle during the etching process. Next, a layer of photoresist is added, this layer allows for the nozzle array to be patterned onto the wafer. Then the photoresist is placed under a mask and then developed, leaving the desired pattern for the nozzle array. The exposed silicon dioxide is then removed. With the base silicon exposed, the etching process creates the desired nozzle array, etching completely through the wafer. The array is separated into smaller arrays and each sample is coated with an aluminum/iron layer to act as a catalyst for CNT growth. The final step of the process is to place the arrays into the CNT furnace then characterize the results.
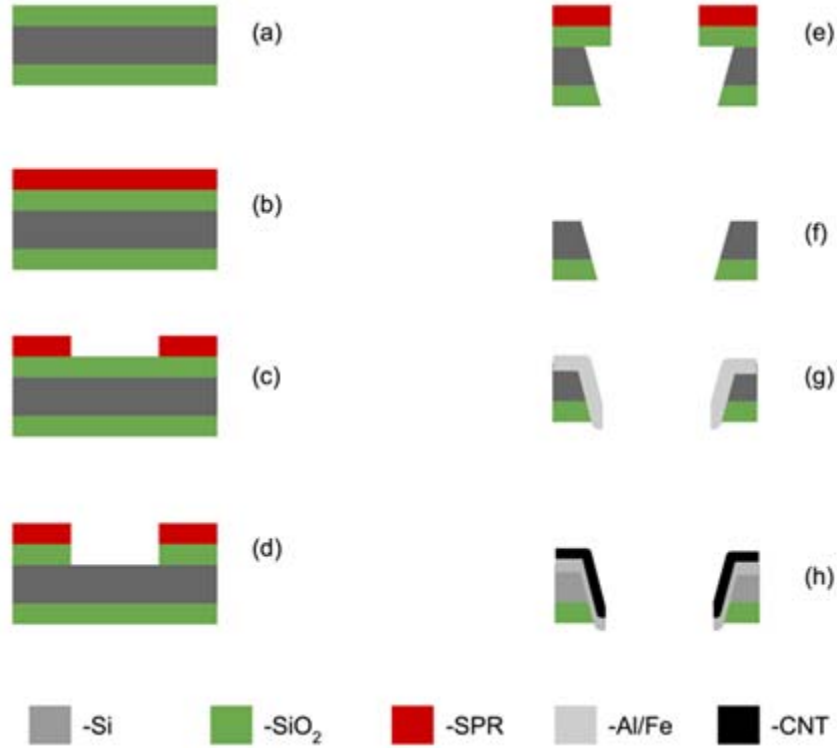
(a) wafer with both sides coated by silicon dioxide; (b) photoresist applied (c) patterned and developed photoresist; (d) removal of unmasked silicon dioxide; (e) etched nozzle; (f) cleaning of top layer of silicon dioxide; (g) catalyst metal deposited; (h) growth of CNTs

Figure 4. Schematic of nozzle fabrication process

B.   PATTERNING PHOTORESIST

The process starts with a blank wafer on which a layer of thermal silicon dioxide is grown. Previous work had not resulted in the desired angled walls of the nozzles, so the decision to use an added layer of silicon dioxide was made to better mask the openings during the etching process. The wafer was then characterized by measuring the thickness of the silicon dioxide layer as well as the total thickness. The next step is to apply the photoresist to the top of the wafer. The photoresist layer functions both as a way to pattern the wafer, creating the nozzle array, and as a second protective mask, in addition to thermal silicon dioxide, during the etching process. The photoresist used in this project

was SPR220-7. When applied under 3000 RPM spin-coating process, resulting film is 7 μm thick [13].

Figure 5 shows the spin coater used in the photoresist application process. The spin coater reaches the desired 3000 rpm with a 15s ramp period then holds at 3000 rpm for another 45 seconds then slowly stopping the rotation. The result is a wafer evenly coated with 8 microns of photo resist, ready for patterning.

Figure 5. Photoresist application—spin coater. Source: [10].

Once a wafer has been coated with photoresist, it is ready to be exposed to UV light through a photolithographic mask. In this project, two different masks, and thus two different nozzle arrays, were used. During the early stages of the project, a mask from a previous thesis was used. It included two nozzle arrays, one 22x16 array of 760μm x 760μm openings and a second 66x50 array of 245μm x 245μm openings. The second mask used was designed by the author and consisted of repeated 5x5 arrays of 450μm x 450μm openings; the total area

of each individual array was 1cm^2. This new design was chosen in order to allow for easier integration into laboratory testing for the nozzle arrays. Each mask consists of a layer of sodalime glass and a chromium layer with the mask design. This mask is placed between the UV light source and the photoresist layer of the wafer in order to pattern the photoresist [14].

The exposure is done inside the contact aligner, shown in Figure 6. With the chromium layer being opaque, only the photoresist directly below the transparent openings in the mask are exposed to the high energy UV light [14]. Thus, when the wafer is submerged in the CD-26 developer, the exposed portions of the photoresist dissolve, leaving exposed silicon dioxide in preparation for etching, and the unexposed portions of the photoresist harden to act as a mask during the etching process [13]. When the photoresist has been properly exposed and developed, the etching process is ready to begin.
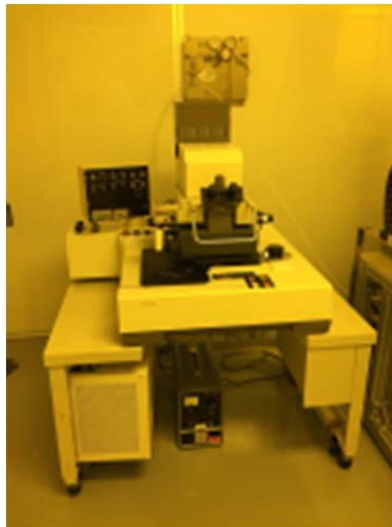

Figure 6. Cannon 501S contact aligner: The instrument used to pattern the photoresist. Source: [10].

C. ETCHING PROCESS

With the added layer of silicon dioxide under the photoresist, an extra step is added prior to the nozzle-etching process. Before the nozzles can be etched

into the silicon wafer, the exposed silicon dioxide has to be removed. This is done via reactive ion etching tetra-fluoro methane (CF_4) and oxygen (O_2).

The wafer is loaded into the Oxford Plasma etcher, shown in Figure 7, the oxide etch process time is adjusted according to thickness of the silicon dioxide layer, and the silicon dioxide removal process begins. Table 1 shows the oxide etch process recipe used in the Oxford Plasma etcher.
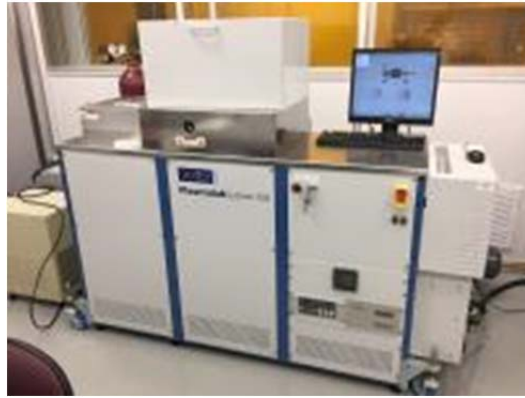
Figure 7. Oxford plasma etcher. Source: [10]

Table 1.   Oxide etch process recipe

Oxide Etch					
Etch Material:	Etch Rate:	Pressure:	Gas Flow:	RF Fwd Power	ICP Fwd Power
SiO_2	100nm/min	20	CF_4:45 O_2:5	100	2000

After the process is complete, the wafer is again characterized: measuring the thickness of the remaining photoresist and verifying that all exposed silicon dioxide has been removed.

Once the silicon dioxide has been removed, the nozzle-etching process can begin. The angled walls are etched using a combination of the process known as Bosch etching and isotropic reactive ion etching [19]. The former process was developed by Robert Bosch GmbH and includes two steps: an

anisotropic etch and an anisotropic deposition to create a bias in the etching direction resulting in a vertical sidewall profile [15]. This two-step process is specifically known as the time-multiplexed deep etching process (TMDE) [15]. The etch step uses biased sulfur-hexafluoride (SF_6) plasma to bombard the silicon wafer with ions in order to initially etch an isotropic channel into the exposed areas of the wafer [15]. The second, deposition/passivation, step uses octa-fluoro-butane (C_4F_8) plasma to form a protective Teflon film on all areas before the next etch [15]. When the cycle repeats, the successive etches preferentially remove the protective film from horizontal surfaces [14]. The result is an anisotropic etch where the etch material is only removed in the vertical direction. These steps are alternated for a given number of repetition cycles to achieve the desired etch depth, with vertical wall. In our process, we call this segment *anisotropic etch* due to the vertical walls (i.e., etching progressing in a single direction). Roxhed et al. showed that a tapered etch was possible by using a TMDE Bosch step combined with an isotropic etch [19]. Following the anisotropic TMDE, the isotropic etch begins [19]. In the isotropic step, the wafer is bombarded using SF_6 plasma for a given time, this time without directional bias, removing the same amount of etch material in all directions. Table 2 shows the specifics of the modified Bosch recipe used in this experiment.

Table 2.   Modified recipe used for angled nozzle etch. Adapted from [19].

Steps:	Time:	Pressure:	Gas Flow:	RF Fwd Power	ICP Fwd Power
Bosch Cycles (10): 0.8µm/cycle					
Anisotropic Etch	8 Seconds	20	C_4F_8:0 SF_6:120	10	1750
Anisotropic Deposition	3 Seconds	12	C_4F_8:140 SF_6:0	7	1750
Isotropic Etch: 2.2µm/min					
Etch	4 min	15	C_4F_8:0 SF_6:100	0	600
Repeat for desired total etch length (typically 5 loops)					

Figure 8 (a) shows the anisotropic etch step: it is based in the vertical direction leaving the sidewalls unaffected. Figure 8 (b) shows the isotropic etch step: unbiased, this step etches in each direction equally deepening and widening the nozzle. Alternating these two steps: A and B, results in a narrowing of the trench towards the bottom of the wafer. Ultimately, the width of the trench at the bottom of the wafer would equal the original width of the opening in the photoresist/SiO$_2$ mask and the width at the top of the wafer would be equal to the original width of the opening of the photoresist plus twice the number of isotropic etches times the amount etched per step (B). This would result in an angled nozzle sidewall. Figure 9 shows a schematic of the repeated steps with an angled sidewall beginning to form.
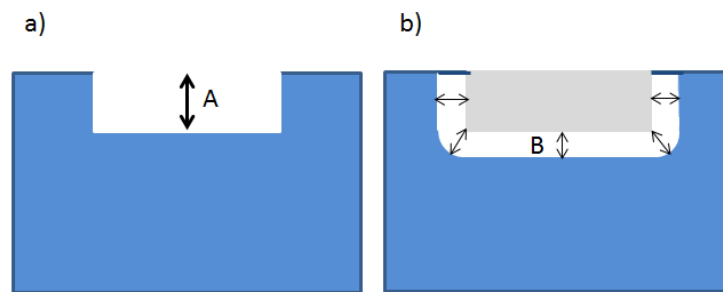

Figure 8. Anisotropic etch (a) and Isotropic etch (b) schematic.
Source: [10]
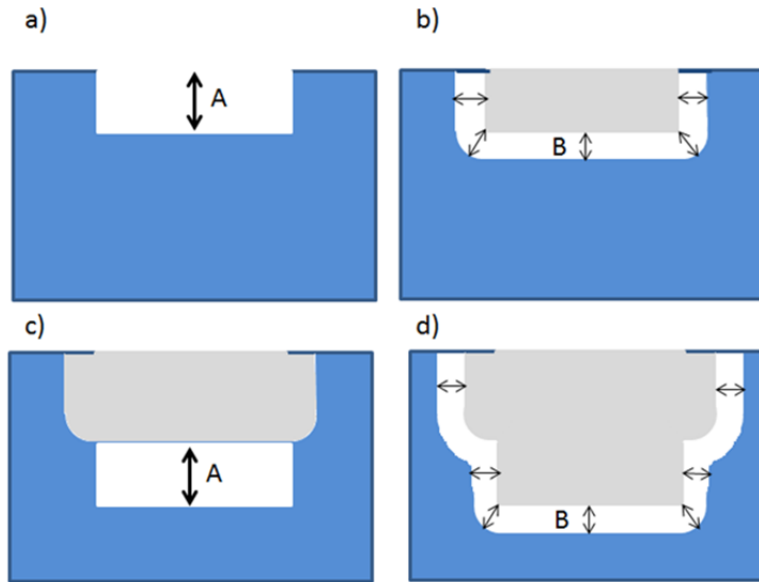
Figure 9. Repeated anisotropic and isotropic etches from Figure 8
showing the formation of angled sidewalls

Once the wafer is etched completely through, there is no more use for the protective masks. This means that the remaining silicon dioxide and photoresist must be removed. In the Oxford etcher, the wafer is used to "seal" the chamber and separate etching plasma from the helium cooling. The presence of holes in the wafer at this point would interfere with that process. Thus, a smaller reactive ion etcher is used in the removal of the two films.

The wafer is loaded into the Trion Plasma etcher shown in Figure 10. The films are removed in top to bottom order. The first to be removed is the photoresist layer. The recipe for this process uses oxygen plasma to bombard the wafer and remove the photoresist while not affecting the already etched nozzles [10]. Table 3 shows the recipe used to remove the photoresist.

Figure 10. Trion plasma etcher used in removal of silicon dioxide and photoresist. Source: [10].

Table 3. Photoresist removal recipe (Trion)

"Clean"					
Etch Material:	Etch Rate:	Pressure:	Gas Flow:	RF Fwd Power	ICP Fwd Power
SPR	1µm/15min	250	CF_4:0 O_2:50	100	N/A

Once the photoresist is removed, an oxide etch recipe (similar to the one used in the Oxford Plasma etcher earlier) is used to remove any remaining silicon dioxide and prepare the wafer for metal deposition. Table 4 shows the recipe used to remove the silicon dioxide.

Table 4. Oxide etch process recipe (Trion)

Oxide etch					
Etch Material:	Etch Rate:	Pressure:	Gas Flow:	RF Fwd Power	ICP Fwd Power
SiO_2	1µm/30min	175	CF_4:50 O_2:0	125	N/A

D.   CNT GROWTH: METAL DEPOSITION AND FURNACE

To achieve CNT growth on the silicon wafers, an adhesion layer and catalyst layer are required on the surface of the wafer [10]. In this project, those layers were iron and aluminum respectively. The adhesion layer is needed because iron will not firmly adhere to silicon; the iron layer could be removed as easily as a coating of dust.

The entire process occurs inside the deposition chamber of the Angstrom COVAP II Metal Evaporator which is indicated by the arrow in Figure 11. The process begins with the solid pellets of source metals being loaded into tungsten boats inside the deposition chamber shown in Figure 12. These tungsten boats are connected to a circuit and during metal deposition, current is run through them, melting the pellets via Joule's heating. During this time, as the pellets are being melted down and begin to evaporate, the shutter is in the closed position, protecting the wafer and not allowing any metal deposition onto the sample. A deposition controller is detecting the rate of deposition of the particular metal (in this project the desired rates were 1 Å/s for aluminum and 0.5 Å/s for iron) and once that rate is reached, the shutter opens and the deposition onto the wafer begins. Once the onboard computer detects that the desired thickness has been deposited, the shutter again closes, protecting the sample and allowing for the precise thickness of metal to be maintained. The closed and opened orientations are shown in Figure 13. As a note of clarification, only one metal is deposited at a time, first aluminum then iron. Once the required thicknesses of each metal have been deposited onto the wafer, the wafer is then ready to go to the CNT furnace.
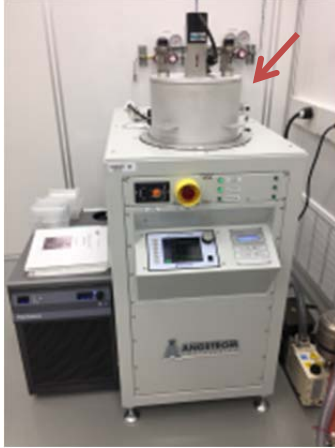
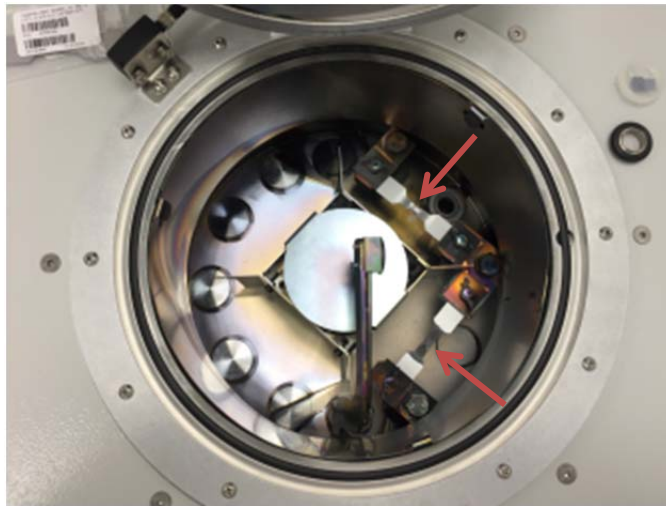Figure 11.   Angstrom COVAP II Metal Evaporator. Source: [10].

Figure 12.   aluminum and iron pellets in tungsten boats inside deposition chamber of the COVAP II. Source: [10].

Figure 13.   Closed and open orientation of protective shutter inside deposition chamber of the COVAP II. Source: [10].

The EasyTube 2000 CNT Furnace, shown in Figure 14, uses thermal chemical vapor deposition (CVD) to grow carbon nanotubes [17]. When the sample is loaded into the furnace, the reactor inside the furnace is purged with argon [17]. The furnace is then heated up to the desired temperature for CNT growth. Previous theses found that the optimal temperature for this particular furnace to grow the desired CNTs is 750 degrees Celsius [17]. When the furnace is at the desired temperature, the sample is soaked for 2 minutes with hydrogen (H2). Following the hydrogen soak ethylene (CH4), a carbon rich gas, is introduced to the chamber. At 750 degrees Celcius, the ethylene is thermally decomposed and begins to grow CNTs on the catalyst layer that was deposited on the sample in the earlier step. The length of the CNTs grown can be varied in several ways, either by changing the time in which the ethylene is in the furnace or changing the flow velocity [17]. Previous theses found a successful recipe for the growth of CNTs and that recipe was repeated in this step. The ethylene flowed in the chamber for a total of 30 seconds followed by another argon purge during the cool down of the wafer [17] [18].

At this point the sample is ready for characterization, analysis, and integration to a laboratory testing set up.

Figure 14.   EasyTube 2000 CNT furnace. Source: [10].

THIS PAGE INTENTIONALLY LEFT BLANK

III. RESULTS

A. NOZZLE ETCHING

A recipe for an angled wall etch was modified from previous work for this thesis. The resulting recipe was a modified recipe from Roxhed, Griss, and Stemme as well as previous theses and consisted of the two steps previously discussed: an isotropic etch and an anisotropic etch [10] [19]. The repetition of the two steps and the respective etch depths are what determines the angle of the sidewalls.

The angle θ created, as shown in Figure 15, is arctangent of the ratio between the transverse etch direction (2 x B) and the vertical etch depth (2 x (A+B)). The number of loops (2) cancels and thus, θ is governed by the equation

$$\theta = \tan^{-1}\left(\frac{B}{A+B}\right),$$ (1)

where A is the distance etched per anisotropic step and B being the distance etched per isotropic etch [10]. The anisotropic step, as made from several Bosch cycles, (10 in the work discussed here) and the isotropic etch is characterized by a specific duration of etching: 4 minutes. Thus, the previous equation can be modified to be more specific to the recipe [10]:

$$\theta = \tan^{-1}\left(\frac{t_i b}{ca + t_i b}\right),$$ (2)

where t_i is the characteristic time of the isotropic etch in minutes, *b* is the isotropic etch rate in μm/min, *c* is the number of Bosch etch cycles, and *a* is the characteristic anisotropic etch rate in μm/cycle [10]. Taking these values from Table 1, the expected angle is 27.6 degrees.
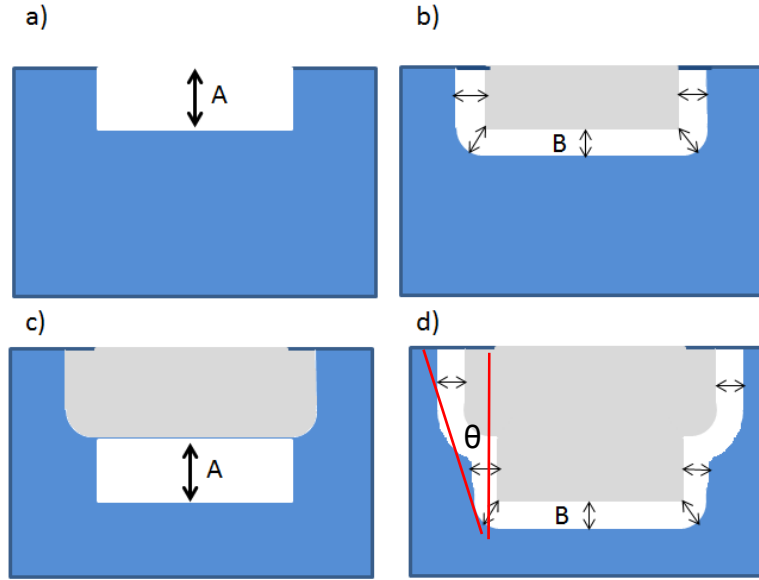
In a) the anisotropic step etches a distance A vertically into the wafer. In b) the isotropic step etches a distance B in every direction in the wafer, the grey area shows the area etched in the first step. Step c) is again the anisotropic step and etches a distance A further into the wafer but only as wide as the original opening. Finally, d) shows a second isotropic etch of distance B in all directions and the angled wall begins to form as well as the method of measuring the angle.

Figure 15.   Diagram of sidewall angle created by alternating anisotropic and isotropic etches. Source [10].

1.   High-density Nozzle Array

The first array that was used to etch the nozzles was from a photolithographic mask used by Brandi Gilbert in a previous thesis. In her work, she was not able to achieve side wall etch with a sufficient angle, but her work provided a valuable information on parameters a, b, c and t_i used in equation (1). A scanning electron microscope (SEM) was used to image the arrays of nozzles following different steps in the nozzle fabrication process.

After placing the wafer in the Oxford Plasma Etcher to begin the nozzle etching process (i.e., after several cycles of the modified Roxhed et al. etch recipe), the sample was removed and cleaved in order to be characterized in the SEM. Figure 16 shows that the recipe was successful in creating angled walls, an early improvement over previous work. It also shows that the separation

between the openings (designed originally for THz imaging arrays) were no
sufficiently apart to provide room for angled walls. This is evident in Figure 17.
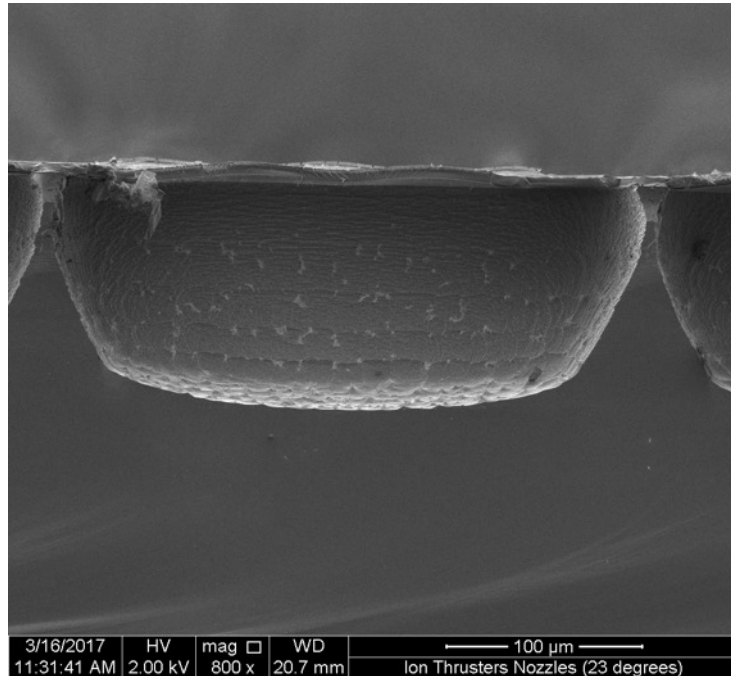
Several cycles alternating between anisotropic steps and isotropic steps result in
an angled sidewall etch. Photo taken after step (e) from Figure 7.

Figure 16.   SEM image of several nozzles partially through the etching
process.
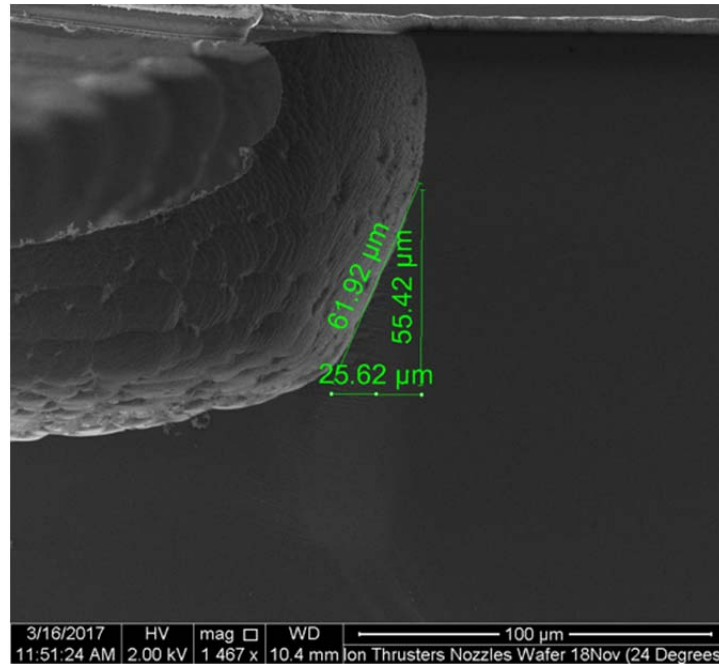
Measurements were done on the SEM to calculate the effective angle of the nozzle.

Figure 17.   Calculation of sidewall angle (24 degrees)

The sidewall angle was measured, as shown in Figure 17, was 24 degrees, 3.6 degrees less than the expected angle of 27.6 degrees. Several reasons could possible explain this, the first being that the Oxford Plasma Etcher is more powerful or effective during one of the steps (most likely the isotropic step) or that the nozzles are arranged too closely and are interfering with each other. The true explanation is a combination of the two, with the latter being evident in the background of Figure 17 (the rear nozzle wall is collapsing into the nozzle behind it).

Despite that design prohibiting the complete etch of a nozzle through the wafer, it was indicative that the choice to include a layer of silicon dioxide was effective in protecting the sidewalls of the nozzle. Figure 18 shows that the mask consisting of layers of SPR20-7 and silicon dioxide remained intact during the etching process. This effect had not been imaged in previous theses and it can

be reasoned that the degradation of the mask layers during the etching process led to the flat walls instead of angled.
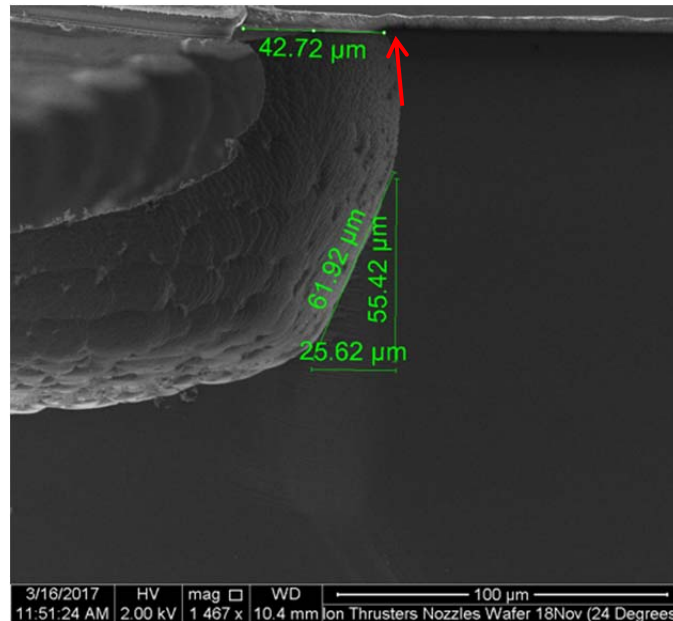
The red arrow points to mask still present after several etch cycles. The layer it is pointing to in the image is the physical structure depicted in green and red in Figure 4.

Figure 18.   SEM Image measuring mask overhang

The next step was to create a new nozzle array that would allow for a complete etch through the wafer.

2.   Low-density Nozzle Array

The high-density mask consisted of two arrays closely packed squares for the nozzles. The new, low-density design consisted of repeated 5x5 arrays of nozzles separated by 1050µm to allow widening during the etching process and arranged to allow for easy cleaving and integration to a lab testing set up. Again, the same angled etch recipe was used with this new array.

As expected, with the greater separation of the openings in the mask used, the nozzles did not interfere with each other and overlap during the etching process. Figure 19 shows the cross-section of one nozzle in the array partially

through the etching process. The iterative nozzles can be seen in the background. Still present is the overhang of the mask that protects the angled sidewalls. However, the separation of the nozzles did not solve the problem of the measured angle being shallower than the expected angle.
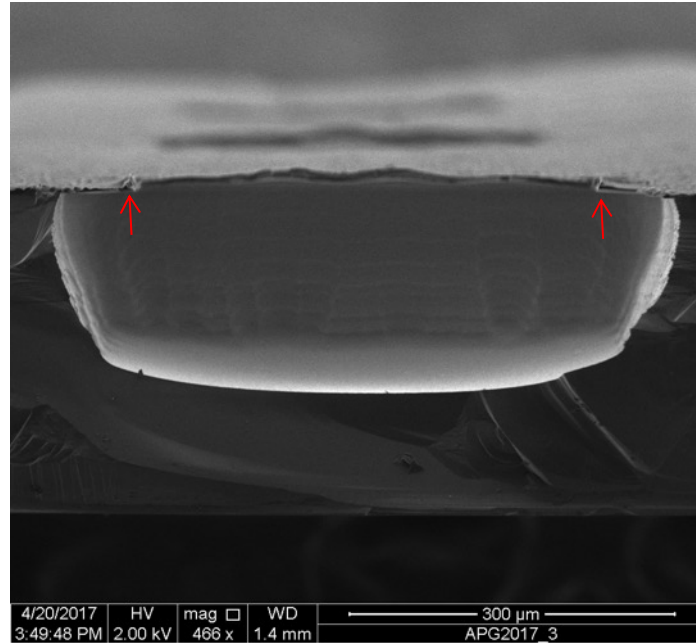
The two red arrows in the figure indicate the overhang that is still present at this point in the etch process.

Figure 19.   SEM image of nozzle using low density array design

Several anomalies are present in Figure 20. Firstly, the measured angle is far less than the expected (20.4 degrees instead of 27.6) and secondly, the non-uniformity of the sidewall towards the bottom of the etch. This is indicative that the problem of the sidewall angle lies heavily in the Oxford Plasma Etcher during the operation of the etch process. This problem can be solved through further characterization of the Oxford Plasma Etcher in follow on work.
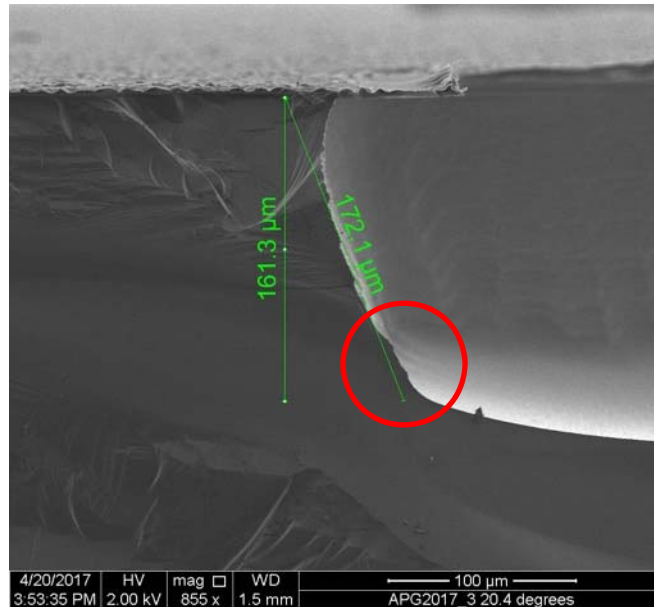
The two measurements shown in green were used to calculate an angle of 20.4 degrees. The red circle highlights an anomaly in the sidewall's angle.

Figure 20.   SEM image of 20.4 degree sidewall

The next step was to attempt a complete etching of the wafer creating angled nozzles with openings on top and bottom. A new wafer was prepared in the same way as those previously discussed. At several points during the etching process the wafer was removed and characterized to insure that the mask was still present and to check on the depth of the nozzle. After twelve full cycles of the recipe, holes began to appear on the bottom of the wafer.

At the point where holes began to appear, the wafer itself had become very fragile and would not survive any further etching. Figure 21 shows an almost fully intact nozzle with a hole through the bottom of the wafer. Had another cycle or two of etching had been conducted, the opening would be square and the size of the original opening in the mask. The wafer was also cleaved in order to measure the resultant sidewall angles of the complete etch.
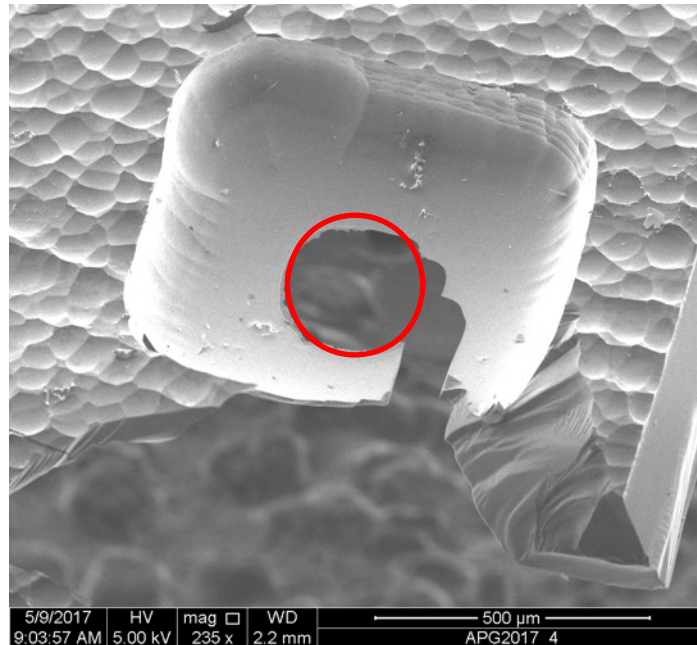
This nozzle was damaged during the cleaving process, but provides a good representation of a nearly-complete nozzle. The red circle represents where the undamaged opening would be.

Figure 21.   SEM image of nearly intact nozzle

Before these images were taken, the mask layer of silicon dioxide and photoresist were removed, thus the overhang visible in previous images is not shown in Figure 22. However, the image shows the success of the etch in the relatively uniformly-angled sidewalls all the way through the wafer. The shallowing of the sidewalls towards the bottom of the nozzle is a result of the opening not being completely formed.

After the completion of the etch, the sidewalls were measured to have an angle of 33 degrees, much closer to the expected angle from the recipe. Figure 23 reflects this and the 166.6µm green line shows how the bottom of the sidewall would look had the opening formed completely.
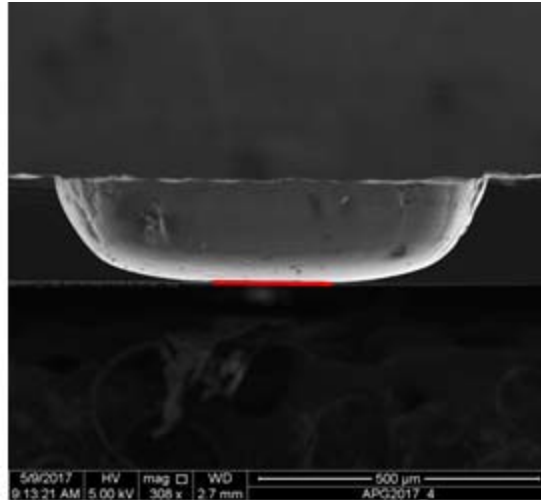
In this cross-sectional view, the opening is not visible, but indicated by the red line.

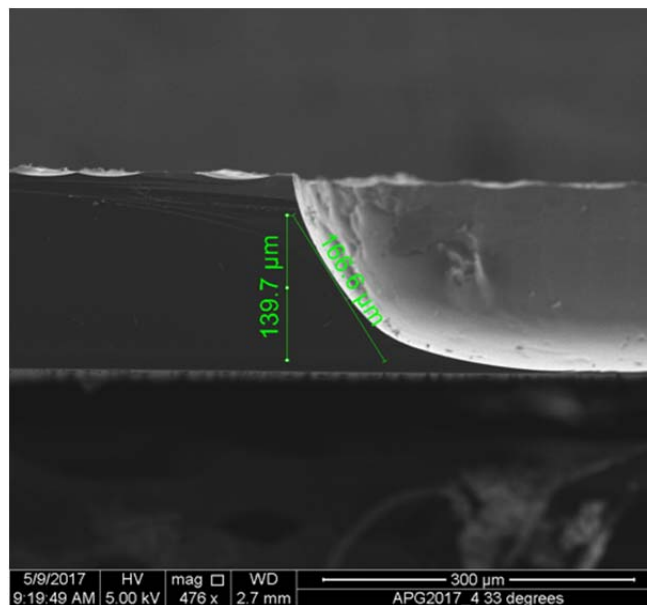Figure 22.   SEM image of complete nozzle cross section

Figure 23.   SEM image: Close up of sidewall showing angle of 33 degrees

The next step in the process was to take the uncleaved samples from the wafer and prepare them for CNT growth. As stated before, the CNTs cannot form

on pure silicon. Thus, an adhesion layer of aluminum and a catalyst layer of iron must be deposited onto the sample before it is put into the CNT furnace. For horizontal surfaces a 10nm and 2.5nm thick layer of aluminum and iron respectively is needed [10]. As previously stated, the adhesion layer of aluminum ensures that the iron used to grow the CNTs firmly bonds to the silicon. However, the sidewalls of the nozzle are not horizontal and the deposition recipe must be adapted based on the estimated angle of the sidewalls (θ).

$$Al\ layer\ thickness\ (nm) = \frac{10}{\sin\theta}$$

$$Fe\ layer\ thickness\ (nm) = \frac{2.5}{\sin\theta}$$

After the metal layers were deposited, an attempt was made to image the metal layer thickness to verify that the correct thicknesses were present on the angled walls. However, due to the capability of the SEM, a clear image was not able to be captured. Operating under the assumption that the correct thicknesses were in fact present, the remaining samples were placed into the CNT furnace. CNTs were grown using the previously discussed 30 second growth recipe at 750 degrees Celsius.

As Figure 24 shows, the CNT growth was successful on the angled side walls. The dark lines present on the walls indicate a separation of the rings of CNTs present along the walls.
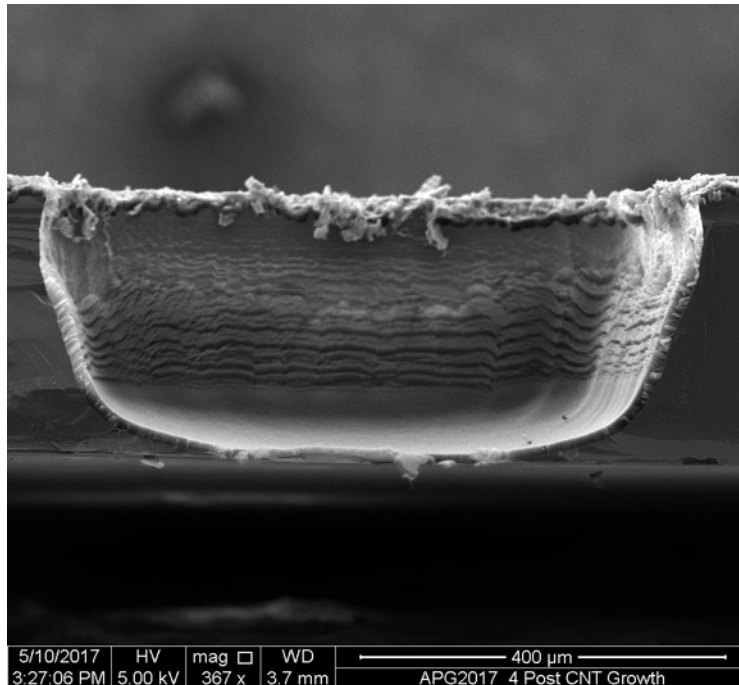
Figure 24.   SEM image: Nozzle cross section after CNT growth

The CNT growth was then characterized in several ways. The first of which, shown in Figure 25 is the length of the CNTs perpendicular to the sidewalls. The average length was found to be around 12µm. This is slightly shorter than the results from previous theses that measured lengths closer to 20µm [10]. This discrepancy is possibly due to the angled sidewalls being slightly sheltered from the flow of ethylene during the growth process. The next way of characterizing the growth was through the metric of ring density, or how many rings per unit length were present on the sidewalls.
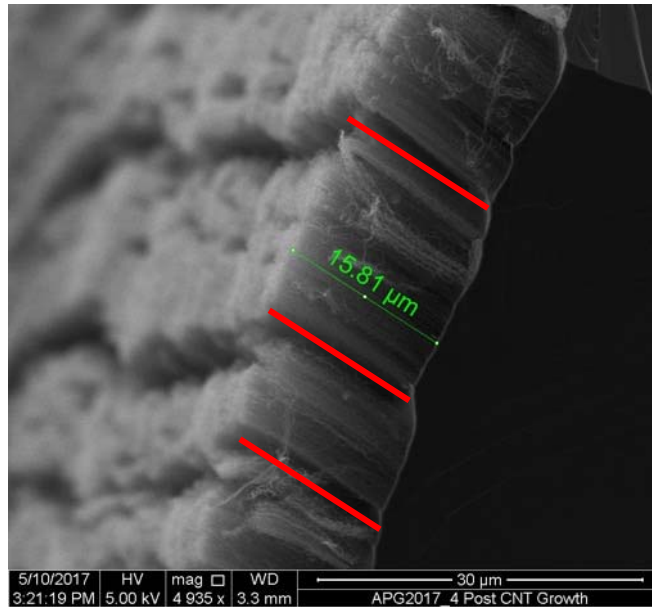
Close up of several rings of CNTs. The red lines represent the separation points.

Figure 25.   SEM image: Measurement of CNT length

Figures 26 and 27 were used to measure the ring density: found to be roughly one ring per 16.45µm. The rings are not completely uniform do to the non-uniformity of the sidewall surface from the etching process, but the average density can be used to form a useful estimate of the Mass Utilization Factor.
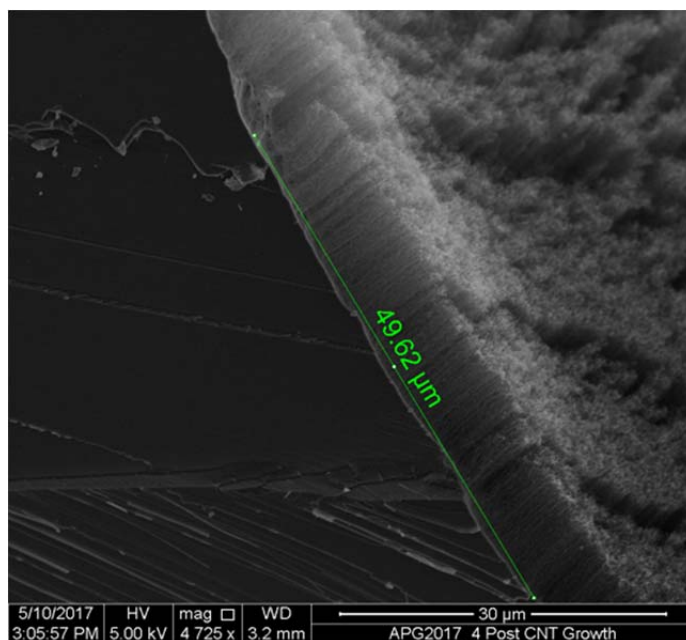
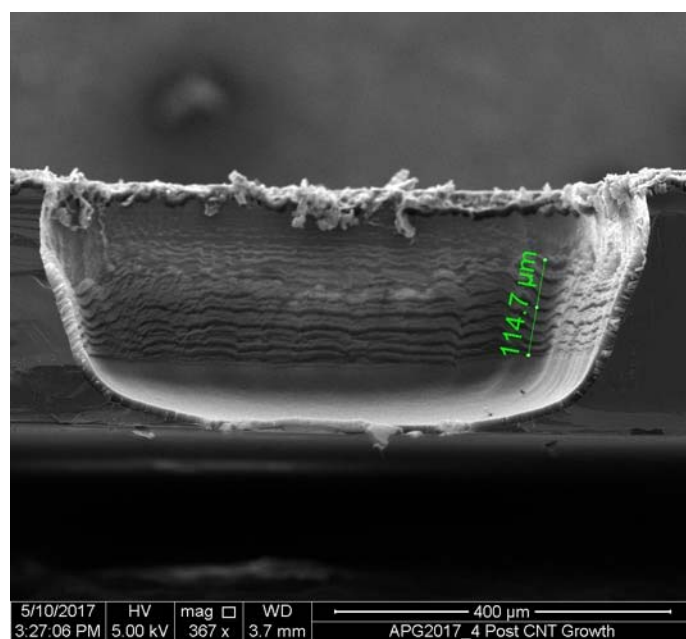Figure 26.   SEM image: Ring density measurement (3 rings)

Figure 27.   SEM image: Ring density measurement (7 rings)

Before creating a general equation for the Mass Utilization Factor of a square nozzle, the Mass Utilization Factor for the sample must be calculated. This is done using the method studied by Gilbert and Ozereko in previous theses

and her calculated value of max ionization distance (21.4nm) [10]. The process is to first calculate the total area of the ionization region, then dividing that area by the total area enclosed by the square ring. The total area of the square ring is the square of its cross-sectional width. It also only assumes that the ring is only one CNT wide [10].

Keeping with the convention of earlier theses and representing the max ionization distance as b_{max} and labelling the cross-sectional width of the ith ring to be d_i the MUF of a square ring is

$$MUF_i = \frac{d_i^2 - (d_i - 2 \times b_{max})^2}{d_i^2}$$

making the total MUF of a nozzle of n rings to be

$$MUF = \sum_{i=1}^{n} MUF_i \times \left(1 - \sum_{l<i} MUF_l\right)$$

With regard to Figure 28, n is equal to 7 and b_{max} is 21.4nm and the widths mentioned in the caption, the total Mass Utilization factor is 0.0464%. While this is much lower that Gilbert's calculated cumulative MUF of 0.164%, the difference in sizes of the openings and the same b_{max} makes the comparison less clear [10]. An easier metric is the percentage increase of total MUF over MUF_1 (the top most ring). In the case of Gilbert's thesis, this percentage increase is 410% and in the case of this project, the percentage increase is 729% [10].
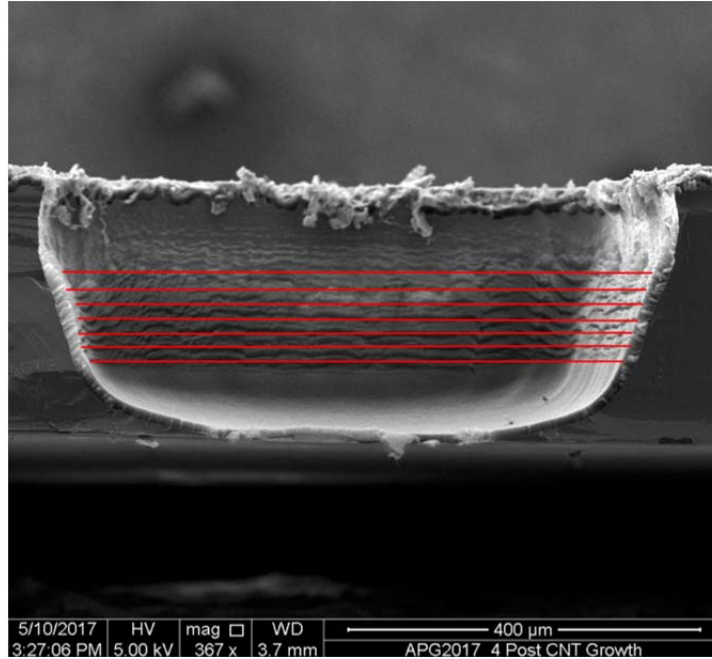
The 7 red lines represent the widths of the 7 rings seen in Figures 23 and 26. From top to bottom the widths are (in μm): 672.9, 663.4, 657.0, 648.3, 635.6, 627.6, and 620.5.

Figure 28.   Re-creation of Figure 23 indicating measurement points

Generalizing the work done in this thesis, it would be useful to calculate the MUF under ideal nozzle conditions. Ideal conditions are considered to be uniform sidewall shape and angle, consistent ring density, uniformity of rings from the top of the nozzle to the bottom, and uniform CNT height. Introducing the constant k for the ring density and referencing to constants labelled in Figure 29, the calculation of the ideal MUF goes as follows:
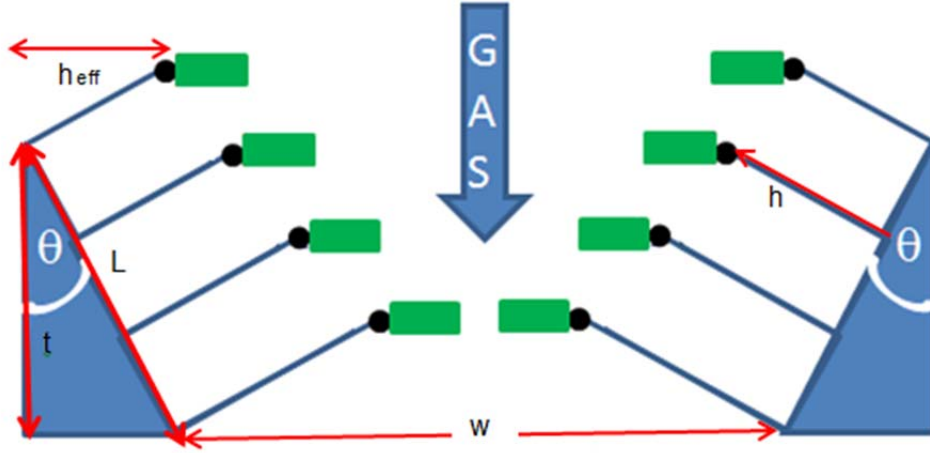
A schematic of an ideal nozzle with the blue lines representing the one CNT wide rings and the ionization areas shown in green. t represents the thickness of the wafer, L = t x tan(θ), w is the initial width of the opening, h is the height of the CNTs, and h_{eff} is the horizontal distance of the CNT tip from the wall of the nozzle

Figure 29.   Ideal nozzle schematic. Adapted from [10].

$$L = \frac{t}{\cos \theta}$$

$$h_{eff} = \frac{h}{\cos \theta}$$

$$n = \lfloor L \times k \rfloor$$

$$d_i = w + 2t \frac{n - i + 1}{n} \tan \theta - 2h_{eff}$$

such that at the top of the nozzle:

$$d_1 = w + 2t \tan \theta - 2h_{eff}$$

plugging back into

$$MUF_i = \frac{d_i^2 - (d_i - 2 \times b_{max})^2}{d_i^2}$$

and

$$MUF = \sum_{i=1}^{n} MUF_i \times \left(1 - \sum_{l < i} MUF_l \right)$$

36

In the case of the nozzle from Figure 27 et al. with a thickness t of 300µm and angle of 33 degrees, the ideal MUF is 0.3%. This ideal value can stand as a benchmark for future iterations of nozzle arrays as the etch recipe is refined and the nozzle arrays begin testing in a laboratory setting.

THIS PAGE INTENTIONALLY LEFT BLANK

IV. CONCLUSIONS

A. CONCLUSIONS

In this thesis, several important benchmarks were set. First, building upon previous thesis work, and angled sidewall was etched into a silicon wafer, providing a formula that can be modified to achieve different angles. Second, that etching process was able to be applied long enough to create a nozzle through the silicon wafer. Third, after successfully growing CNTs on the angled side walls of the nozzle, a Mass Utilization Factor was calculated from the etched nozzle. Lastly, a method for calculating an "ideal" MUF (based on current modelling) was fashioned to provide a baseline comparison to future laboratory testing.

B. FUTURE WORK

This thesis leaves several paths for future work. The equation used to predict the angle of the sidewall needs to be updated and calibrated to the Oxford etcher to provide a better estimate of the recipe outcome. Also, the current method of assuming one CNT per ring needs to be updated to provide a more realistic measurement for the MUF. As shown in Chapter III, the bottom opening of the nozzles is not completely formed. In the next iteration of this project, the bottom layer of silicon dioxide needs to be removed to show a complete square opening equal to the opening in the mask. This would set the stage for the ultimate goal of introducing these nozzle arrays into a laboratory setting and measuring the true MUF and then comparing that result to the calculated and ideal MUF, then iterating the process to improve the efficiency and ability of the design.

THIS PAGE INTENTIONALLY LEFT BLANK

LIST OF REFERENCES

[1]   D. M. Goebel and I. Katz. (2008). Fundamentals of electric propulsion: Ion and Hall thrusters. [Online]. Available: http://descanso.jpl.nasa.gov/ SciTechBook/series1/Goebel__cmprsd_opt.pdf

[2]   E. Y. Choueiri, "A critical history of electric propulsion: The first 50 years (1906-1956)," *Journal of Propulsion and Power*, vol. 20, no. 2, pp. 193–203, Mar-Apr 2004.

[3]   M. Brain. (2006, Nov. 26). How television works. [Online]. Available: http://electronics.howstuffworks.com/tv3.htm

[4]   G. P. Sutton, O. Biblarz, "Electric Propulsion," in *Rocket Propulsion Elements*, 8th ed. Hoboken, NJ: John Wiley & Sons Inc, 2010, pp. 622–672.

[5]   R. C. Olsen. (1987, Feb. 9). Electron beam experiments at high altitudes. *J. Electrostatics*. [Online]. 20(1). pp. 43–57. Available: http://torpedo.nrl.navy.mil.libproxy.nps.edu/tu/ps/doc.html?dsn=11555561

[6]   J. S. Sovey, V. K. Rawlin, M. J. Patterson. (2001, May-Jun.). Ion propulsion development projects in U. S.: Space electric rocket test I to Deep Space 1. *J. Propulsion Power*. [Online]. 17(5). pp. 517–526. Available: http://arc.aiaa.org.libproxy.nps.edu/doi/pdf/10.2514/2.5806

[7]   Deep Space 1 NASA new millennium program technology demonstration spacecraft (2015). Orbital ATK. [Online]. Available: https://www.orbitalatk.com/space-systems/science-national-security-satellites/science-environment-satellites/docs/ FS007_11_OA_3862%20DS1.pdf

[8]   Welcome to the Dawn mission!. (n.d.). NASA. [Online]. Available: http://dawn.jpl.nasa.gov/mission/. Accessed Nov. 1, 2016.

[9]   Dawn spacecraft and instruments (2015, Jul. 30). NASA. [Online]. Available: https://www.nasa.gov/mission_pages/dawn/spacecraft/ index.html

[10]   B. L. Gilbert, "Effect of angled-wall etch design on CNT growth and propellant ionization," M.S. thesis, Dept. Phys., Naval Postgraduate School, Monterey, CA, 2016.

[11]　J. M. Ozereko, "Carbon nanotube enhancement for miniaturized ion thrusters," M.S. thesis, Dept. Astro. Eng., Naval Postgraduate School, Monterey, CA, 2015.

[13]　Megaposit SPR 220 series photoresists, 2 ed., Rohm and Hass., Philadelphia, PA., 2004. [Online]. Available: http://cnm2.engineering.ucdavis.edu/wp-content/uploads/sites/11/2013/05/ SPR220_Data_Sheet.pdf

[14]　C. Liu, *Foundations of MEMS,* 2nd ed. Upper Saddle River, Prentice Hall 2012, ch. 2, pp. 33–69.

[15]　D. Li. (2015). Encyclopedia of Microfluidics and Nanofluidics. [Online]. Available: http://link.springer.com/referenceworkentry/10.1007/978-1-4614-5491-5_200283

[16]　A. Reis and R. Bhattacharya. (2004, Mar.). Deep reactive ion etching (DRIE). ENEE416. [Online]. Available: http://www.ece.umd.edu/class/ enee416.S2004/report6.pdf

[17]　A. D. Wold, "Carbon nanotube electrode development for ion thruster miniaturization," M.S. thesis, Dept. Phy. & Dept. Space Sys. Ops., naval Postgraduate School, Monterey, CA, 2011.

[18]　B. R. Baker, "Development of carbon nanotube films for ion thruster applications," M.S. thesis, Dept. Space Sys. Ops., Naval Postgraduate School, Monterey, CA, 2015.

[19]　N. Roxhed, P. Griss and G. Stemme. (2007, Apr. 24). A method for tapered deep reactive ion etching using a modified Bosch process. *J. Micromech. Microeng*. [Online]. 17(5). pp. 1087–1092. Available: http://iopscience.iop.org/article/10.1088/0960-1317/17/5/031/pdf

[12]　R. D. Doak. (2004, Jul. 9). The assessment of field ionization detectors for molecular beam use. *J. Phys.: Condens. Matter*. [Online]. 16(29). pp. S2863-S2878. Available: http://iopscience.iop.org/article/10.1088/0953-8984/16/29/002/meta;jsessionid= DEDFE69BD31AFEB2386CEE00736E994D.c4.iopscience.cld.iop.org

INITIAL DISTRIBUTION LIST

1. Defense Technical Information Center
   Ft. Belvoir, Virginia

2. Dudley Knox Library
   Naval Postgraduate School
   Monterey, California